

Massive Vacancy Concentration Yields Strong Room-Temperature Ferromagnetism in Two-Dimensional ZnO

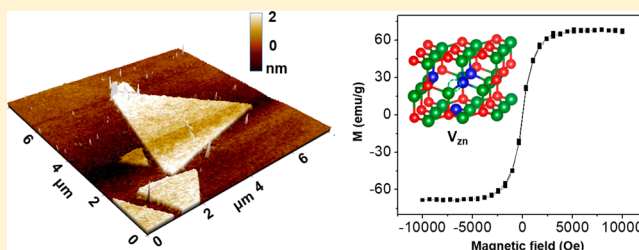
Xin Yin,[†] Yizhan Wang,[†] Ryan Jacobs,[†] Yeqi Shi, Izabela Szlufarska,[‡] Dane Morgan,[‡] and Xudong Wang*[‡]

Department of Materials Science and Engineering, University of Wisconsin-Madison, Madison, Wisconsin 53706, United States

S Supporting Information

ABSTRACT: Two-dimensional (2D) ZnO nanosheets with highly concentrated Zn vacancies (V_{Zn}) of up to approximately 33% were synthesized by ionic layer epitaxy at the water–toluene interface. This high cation vacancy concentration is unprecedented for ZnO and may provide unique opportunities to realize exotic properties not attainable in the conventional bulk form. After annealing, the nanosheets showed characteristic magnetic hysteresis with saturation magnetization of 57.2 emu/g at 5 K and 50.9 emu/g at room temperature. This value is 1 order of magnitude higher than other ZnO nanostructures and comparable to the conventional ferrimagnetic Fe_3O_4 . Density functional theory calculations, with the support of experimental results, suggest that a high concentration of V_{Zn} (approximately one-third of the Zn sites) can form spontaneously during synthesis when stabilized by H ions, and the formation of V_{Zn} could be further facilitated by the presence of grain boundaries. It is essential to remove the H for the nanosheets to show ferromagnetism. The mechanisms identified for the origin of the high magnetism in ZnO nanosheets presents an intriguing example of a kinetically stabilized, non-equilibrium, highly defective 2D nanomaterial with a significantly enhanced physical property.

KEYWORDS: Defect engineering, non-equilibrium, non-layered metal oxide, ferromagnetism, ionic layer epitaxy



Point defects, such as vacancies or interstitials, are an essential factor that determine the physical properties of materials.^{1,2} The ability to control and manipulate point defects in materials synthesis and processing has been a fundamental strategy to achieve numerous desired optical, electrical, and magnetic functionalities.³ Nevertheless, the concentration of defects are usually restricted to relatively low levels by thermodynamics (e.g., due to high formation energy) or kinetics (e.g., due to slow growth rates).^{4,5} Irregular defect types or high defect concentrations, though often predicted to enable exotic properties, are often associated with metastable states that are far from equilibrium.^{6,7} For example, room-temperature ferromagnetism, discovered in ZnO due to the zinc vacancy (V_{Zn})-induced spin polarization of the top of the valence band,^{8–15} is intriguing for multiproperty coupling. However, the amplitude of ferromagnetism is generally very weak due to the limited V_{Zn} concentration in the material lattice. While extremely high oxygen vacancy concentrations (e.g., >15% on a sublattice) have been found in some oxides (e.g., perovskite $Ba_{0.5}Sr_{0.5}Co_{0.8}Fe_{0.2}O_{3-\delta}$ can support over 25% V_O on the oxygen sublattice), they are generally associated with quite straightforward charge balancing of different valence cations, and interestingly, there are no large cation vacancy equivalents of which we are aware. It has therefore been viewed as impractical to engineer large oxide cation defect concentrations in general, and essentially impossible in a material without active redox centers like transition metals.

However, this work shows that a strong cooperative coupling phenomenon can stabilize a massive >30% defect concentration in nanoscale ZnO, enabling the design of a dramatically stronger ZnO ferromagnet and potentially many new highly cation defected oxides.^{16–20}

The recently developed ionic layer epitaxy (ILE) is a kinetically controlled synthesis approach that uses an amphiphilic monolayer to direct the nucleation and crystal growth within a two-dimensional (2D) space and thus creates monocrystalline oxide nanosheets with thickness at $\sim 1\text{--}2$ nm.^{21,22} This unique growth approach to 2D oxides brings new opportunities to control the evolution of defects within a quasi-2D crystal lattice, which may enable new ways to achieve a wide array of material properties. In this work, we report the creation of polycrystalline ZnO nanosheets with an average thickness of ~ 1.8 nm that have exceptional magnetic properties enabled by an unprecedented Zn vacancy (V_{Zn}) concentration of up to approximately 33%. The materials are grown by introducing a water–oil interface in ILE. After annealing in argon, these nanosheets exhibited strong saturation magnetization M_s at both 5 K (57.2 emu/g) and room temperature (50.9 emu/g). Additional monocrystalline ZnO nanosheets, grown by ILE at the water–air interface,

Received: June 25, 2019

Revised: August 23, 2019

Published: September 16, 2019

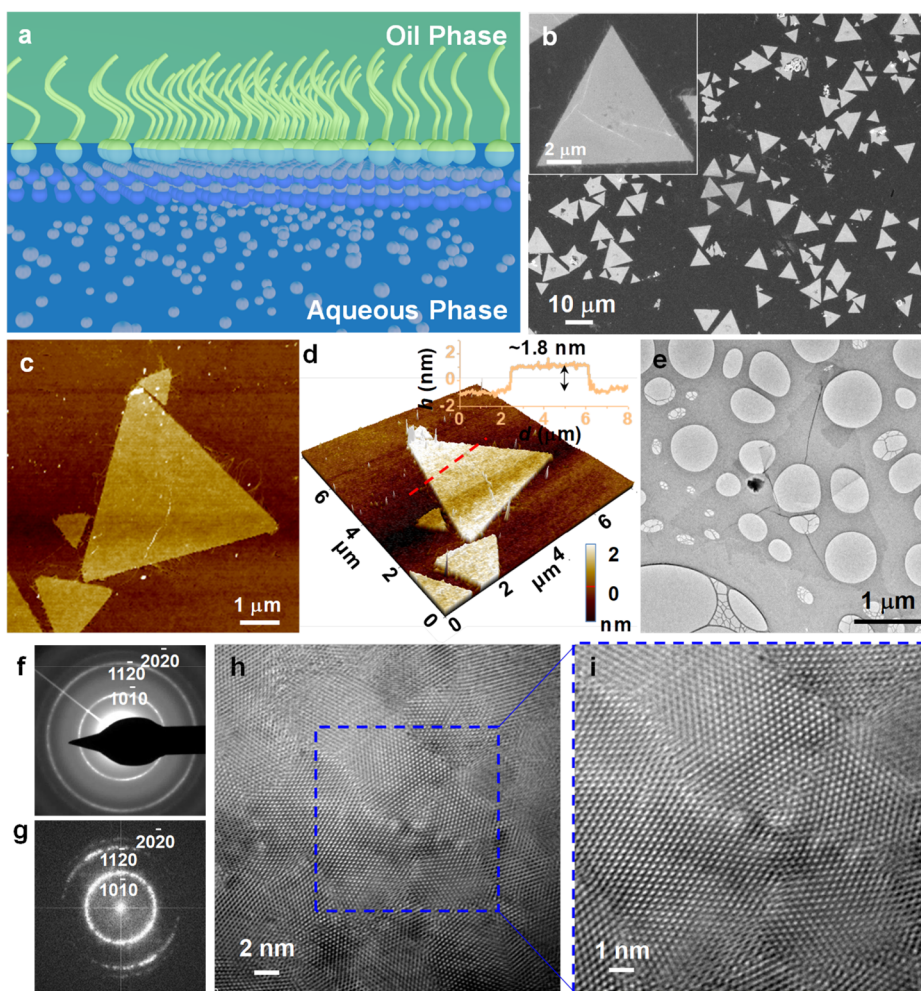


Figure 1. Morphology and crystal structure of ZnO nanosheets grown at a water–oil interface. (a) Schematic of the ILE ZnO nanosheet growth at a water–oil interface. (b) A large-scale SEM image showing as-synthesized ZnO nanosheets supported on a Si substrate. Inset is a single triangular nanosheet. (c) AFM topography image showing the flat surface. (d) The corresponding 3D AFM image of the same nanosheet in (c). Inset is the height profile along the red dashed line revealing the thickness to be 1.8 nm. (e) Low-magnification TEM image showing one nanosheet rested on a holey carbon TEM grid. The concentric diffraction rings indicate the nanosheet is polycrystalline. (f) A FFT pattern of the nanosheet lattice shown in h. (g) HRTEM image showing the polycrystalline crystal lattice of wurtzite ZnO. (i) Enlarged TEM image showing the clean and sharp grain boundaries.

exhibited a smaller (than polycrystalline) yet still very high M_s of 37.2 emu/g. The strong ferromagnetism was attributed to the stabilization of a very high V_{Zn} concentration as a result of H-passivation as suggested by density functional theory (DFT) calculations and confirmed with electron energy loss spectroscopy (EELS) measurements. DFT calculations further suggested that grain boundaries aid in the formation of additional V_{Zn} . Obtaining such a high V_{Zn} concentration likely resulted from the fast kinetics of the ILE growth process and the ultrathin nature of the ZnO nanosheets.

Highly defective ZnO nanosheets with strong room-temperature ferromagnetism were enabled by ILE using a new water–oil interface instead of the conventionally used water–air interface (the details of the synthesis are included in the [Experimental Section](#)). As schematically shown in [Figure 1a](#), the water–oil interface was formed by using an aqueous ZnO nutrient solution as the water phase and toluene as the oil phase. The surfactant monolayer of sodium oleylsulfate ($\text{NaO}_4\text{SC}_{18}\text{H}_{35}$) stabilized itself at the water–oil interface by keeping the hydrophilic head groups in the water phase and the hydrophobic tails in the oil phase. The ionized surfactants

were negatively charged and attracted the positively charged Zn^{2+} cations to form a concentrated ionic layer underneath the headgroups. The monolayer then served as a template to direct the nucleation and growth of the nanosheets within the concentrated Zn^{2+} layer. Similar to the growth results from typical water–air ILE, the as-prepared ZnO nanosheets all had a triangular shape with sharp and equal-length edges ([Figure 1b](#)). Most nanosheets exhibited a side length of $\sim 10 \mu\text{m}$, while smaller nanosheets with sizes of 2–3 μm were also observed. The atomic force microscopy (AFM) topography image in [Figure 1c](#) demonstrates the uniform thickness across the entire nanosheet, which was measured to be $\sim 1.8 \pm 0.2 \text{ nm}$. One significant outcome from the water–oil interface ILE is the very clean surfaces with fewer particles and surface additives as compared to the water–air interface growth. This feature can be clearly observed from the 3D topography shown in [Figure 1d](#). The improved growth cleanness can be attributed to the less dynamic water–oil interface at the growth temperature (60 °C) compared to the water–air interface.

The crystal structure of the nanosheets grown at the water–oil interface was analyzed by electron microscopy. [Figure 1e](#)

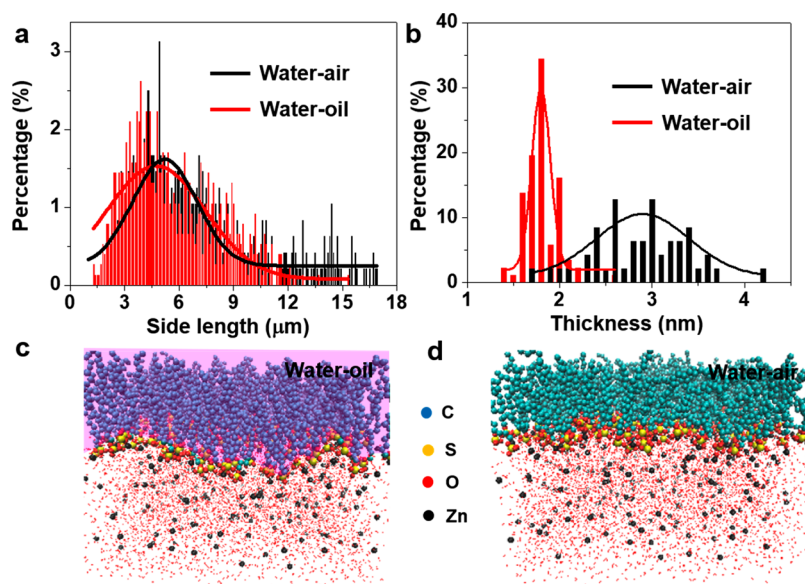


Figure 2. Growth comparison between the water–air and water–oil interfaces. (a) Size distribution and (b) thickness distribution of the nanosheets grown at water–air and water–oil interface. (c and d) MD simulation generated Zn^{2+} ion distribution at (c) water–air and (d) water–oil interfaces.

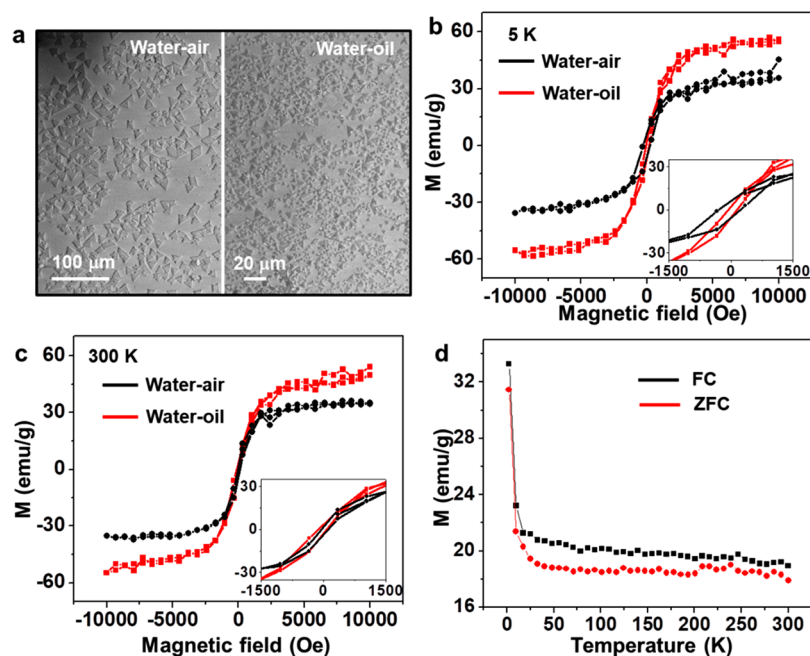


Figure 3. Magnetic property of ZnO nanosheets. (a) Large-scale SEM images of ZnO nanosheets grown at the water–air interface (left) and water–oil interface (right) on sapphire substrates. (b and c) Magnetization curves of the nanosheets at the water–air and water–oil interface at (b) 5 K and (c) 300 K. The insets show the enlarged hysteresis loops. (d) ZFC and FC curves of the nanosheets at the water–oil interface as a function of temperature from 5 to 300 K. The applied magnetic field was 500 Oe.

shows a low-magnification transmission electron microscopy (TEM) image of an individual nanosheet resting on a holey carbon TEM grid. A striking feature from these nanosheets was their polycrystalline structure, as revealed by the concentric diffraction rings from the selected area electron diffraction (SAED) (Figure 1f), which was completely different from the single-crystalline structure of the nanosheets obtained at the water–air interface. The concentric diffraction rings were indexed to $\{10\bar{1}0\}$, $\{11\bar{2}0\}$, and $\{20\bar{2}0\}$, the same as the fast Fourier transfer (FFT) pattern (Figure 1g), matching well to the JCPDS card (no. 36-1451), confirming the hexagonal

wurtzite structure. The high-resolution TEM (HRTEM) image in Figure 1h clearly shows the polycrystalline film structure, where the irregular crystalline domains had sizes of ~ 10 nm on average. A closer observation in Figure 1i revealed the clean wurtzite lattices of all the domains with exposed (0001) surface. The domain boundaries were sharp, and no amorphous phase could be found in between. Formation of the polycrystalline structures with triangular shape could be attributed to the synergic effect of ordered surfactants packing^{23–25} and the higher steric hindrance provided by the oil phase. The formation of single-crystalline nanosheets is a

Table 1. Comparison of Magnetic Property of ZnO Nanosheets with Other ZnO Nanostructures and Other Materials

materials	saturation magnetization (M_s)			T_c	ref
	emu g ⁻¹	emu cm ⁻²	emu cm ⁻³		
ZnO nanosheets (air)	37.2	6.02×10^{-5}	208.5	>RT	this work
ZnO nanosheets (oil)	57.2	5.77×10^{-5}	320.7	>RT	this work
pure ZnO nanorods	2×10^{-4}			>RT	Wang et al. ²⁶
pure ZnO nanoparticles	0.002			>RT	Garcia et al. ²⁷
fine grained (~30 nm) ZnO film			8.3	>RT	Tietze et al. ⁵¹
Mn-doped ZnO thin film	0.05			>RT	Sharma et al. ²⁸
pulsed-laser deposited pure ZnO thin film	1.3×10^{-2}			>RT	Khalid et al. ⁹
magnetron-sputtered ZnO thin film	0.62			>RT	Kapilashrami et al. ¹²
ZnO nanoplates	10^{-1}			>RT	Hong et al. ⁵²
ZnO nanostructure arrays	6.1			>RT	Li et al. ²⁹
Fe ₃ O ₄ nanoparticles	61.4			>RT	Wei et al. ³²
Fe-doped SnS ₂ monolayer	3.49×10^{-3}			31 K	Li et al. ³¹
Cr ₂ Ge ₂ Te ₆ bilayer	$\sim 10^{-3}$ emu			30 K	Gong et al. ⁵³
MnSe _x monolayer		$\sim 3.3 \times 10^{-5}$		>RT	O'Hara et al. ³⁰
VSe ₂ monolayer			~ 2700	>RT	Bonilla et al. ⁵⁴

result of free rotation of crystallites as they merge via the oriented attachment mechanism,²¹ where the surfactant tails in air had a much lower energy barrier for lateral movement.

In order to obtain a better understanding of the influence of the oil phase on the nanosheet structure and morphology, a statistical analysis was performed on the geometry of nanosheets grown at both the water–oil and water–air interfaces (typical images of nanosheets grown at water–air interface were included in Figure S1). The size distributions, which were represented by the side length, are plotted in Figure 2a. For each of the curves, more than 1000 nanosheets were measured. Both curves in Figure 2a show a Gaussian distribution with a long tail toward larger sizes. When grown at the water–air interface, the size ranged from 1.5 to 17.5 μm with the peak position at 5.4 μm . The nanosheets grown at the water–oil interface exhibited a slightly narrower size distribution (1.5 to 12.0 μm) with the peak position at 4.8 μm . The thickness difference of the nanosheets grown from both interfaces was more obvious (Figure 2b). The samples from the water–oil interface exhibited a narrow distribution from 1.6 to 2.1 nm with the peak position at 1.8 nm. By comparison, the thickness of the water–air interface nanosheets was larger and ranged from 1.7 to 4.2 nm with the peak position at 2.9 nm.

Molecular dynamics (MD) simulations were used to further understand how the surfactant–oil phase interaction influences the nanosheet growth. The simulated packing of the surfactant molecules at both the water–oil and water–air interfaces is shown in Figure 2c,d, respectively. With the same surfactant density and Zn²⁺ ion concentration, the surfactant monolayer at the water–oil interface exhibits a relatively higher roughness compared to the water–air interface, as surfactants are pulled more toward the oil phase. This might be the reason that the water–oil interface yielded smaller nanosheets. Due to the larger roughness of the surfactant monolayer at the water–oil interface, the charge distribution perpendicular to water surface became wider than that at the water–air interface under the same surfactant concentration. Therefore, given the total charge for both systems is the same, the charge density at water–oil interface is lower at the same depth from the interface compared to the air–water interface, which yields a narrower Stern layer of Zn²⁺ (Figure S2). As a result, thinner nanosheets with a narrower thickness distribution were

obtained from the water–oil interface. This understanding is validated by comparing the resultant nanosheet thicknesses from the use of other oil phases as detailed in the Supporting Information (Figures S3–S5).

The ferromagnetic properties of the ZnO nanosheets were studied with a superconducting quantum interference device (SQUID). The as-synthesized nanosheets showed no ferromagnetism (Figure S6). However, after being annealed in argon at 400 °C for 1 h (Figure 3a and Figures S7–S10), strong ferromagnetism was discovered from both samples at 5 and 300 K, as shown in Figure 3b,c. The polycrystalline ZnO nanosheets grown at the water–oil interface showed a M_s of 57.2 ± 6.4 emu/g at 5 K and 50.9 ± 5.7 emu/g at 300 K. As a comparison, the single-crystalline ZnO nanosheets grown at the water–air interface showed smaller M_s of 37.2 ± 6.7 emu/g at 5 K and 35.0 ± 6.3 emu/g at 300 K. The small difference of M_s at 5 and 300 K suggests the ferromagnetism is robust against thermal fluctuations in the range of 5 to about 300 K. The temperature-dependent magnetization is further probed by the zero field cooled (ZFC) and field cooled (FC) measurements. As shown in Figure 3d, the non-zero difference between ZFC and FC curves from 5 to 300 K further supports the existence of room-temperature ferromagnetism. Normalized by the total weight of the ZnO nanosheets (by using the theoretical ZnO bulk density of 5.61 g/cm³), the M_s values measured in this work were quantified and compared to relevant materials, as summarized in Table 1. First of all, M_s values of ZnO nanosheets in this work were one to 5 orders of magnitude higher than those being reported on other ZnO nanostructures.^{26–29} The M_s values are also comparable or even higher than most state-of-the-art magnetic 2D materials (e.g., Fe-doped SnS₂, MnSe₂)^{30,31} as well as conventional ferrimagnetic materials, like Fe₃O₄ nanoparticles (61.4 emu/g).³²

Ferromagnetism in undoped ZnO has been shown to originate from Zn vacancies (V_{Zn}) both from experiments^{8,12,33–35} and DFT studies,^{13,14,36–39} however we find that in order to explain the ferromagnetism measured in our experiments, a large concentration of vacancies would be required. Assuming that the ferromagnetism in ZnO originates from V_{Zn} , each V_{Zn} in the bulk is expected to contribute $2 \mu_B$ to the total magnetization based on our present DFT calculations (see Supporting Information for more details). Therefore, a

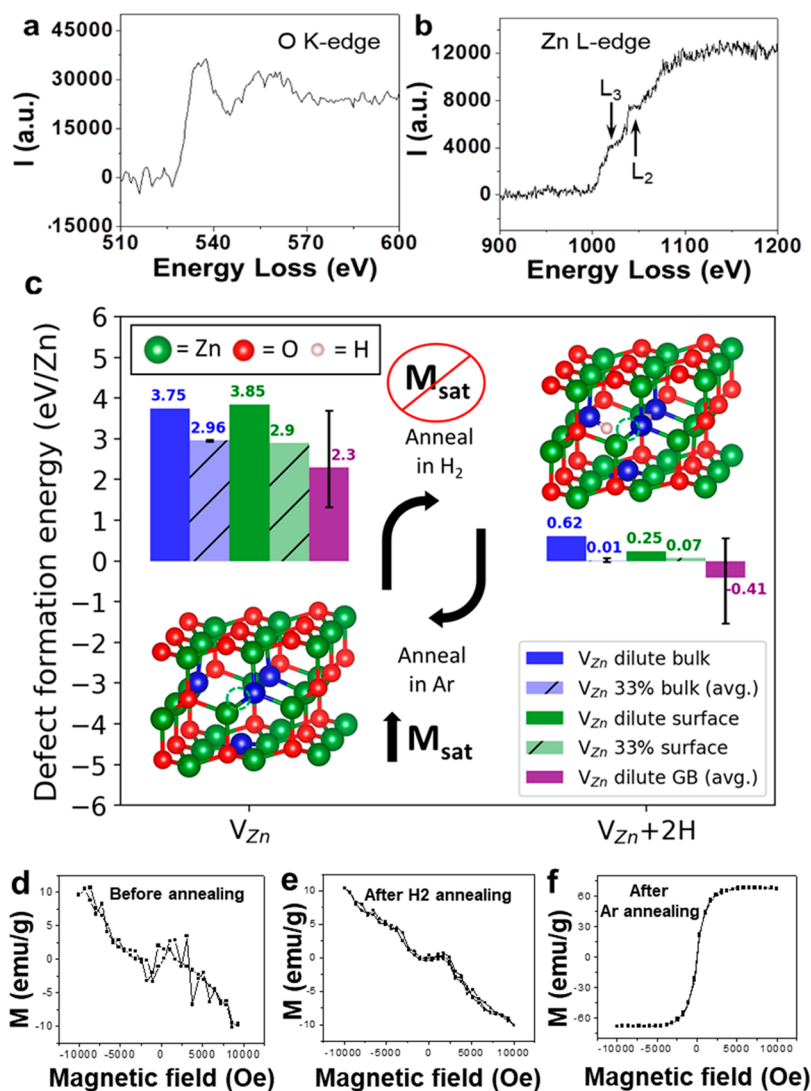


Figure 4. Magnetization mechanism investigation. (a and b) EELS spectra of (a) O K-edge and (b) Zn L-edge to estimate the Zn:O ratio in the nanosheet. The Zn:O ratio was found to be around 2:3. (c) Summary of key findings from DFT calculations of dilute and highly concentrated 33% unpassivated V_{Zn} and passivated $V_{Zn} + 2H$ defects in various ZnO bulk, surface, and grain boundary structures. The blue, green, and purple bars denote the formation energy of bulk, surface, and grain boundaries, respectively. The solid and hashed bars denote defect formation energies of dilute and 33% V_{Zn} , respectively. The numbers next to the bars denote the defect formation energy values (as eV/ V_{Zn}), where for the dilute V_{Zn} in grain boundaries and 33% V_{Zn} in the bulk, these values are averages over six grain boundary structures and three (unpassivated V_{Zn}) and four (passivated V_{Zn}) 33% V_{Zn} bulk arrangements, respectively. The error bars denote the maximum and minimum values from the set of averaged defect formation energies. For the bulk 33% passivated V_{Zn} case, two arrangements were found to have a negative formation energy of -0.02 eV/ V_{Zn} , indicating their formation is thermodynamically stable. The circular arrows in the middle signify the resulting magnetic behavior under H₂ annealing (H passivates V_{Zn} and removes magnetic moment) and under Ar annealing (H is removed from V_{Zn} , creating a magnetic moment). (d–f) M – H curves of the nanosheets showing no ferromagnetism properties either (d) as-synthesized (before Ar annealing) or (e) after ferromagnetic nanosheets were subsequently annealed in H₂. Note that ferromagnetism was observed when the as-synthesized nanosheets were annealed in Ar (f).

magnetization of 50 emu/g requires an average V_{Zn} concentration of about 36%. To evaluate if the nanosheet V_{Zn} concentration is consistent with the high value implied by this magnetization mechanism, electron energy loss spectroscopy (EELS) was performed to investigate the stoichiometry of ZnO nanosheets. Elemental data were collected at the cross section of nanosheets to minimize the potential contribution from surface adsorbed H₂O or O₂ molecules (Figure S11). As shown in Figure 4a,b, strong characteristic peaks of O K-edge at 537.6 and 558.0 eV and Zn L-edge at 1019.7 and 1047.4 eV were obtained. From the Zn and O characteristic peaks, the Zn:O ratio was calculated to be approximately 2:3, which is

qualitatively consistent with the expected V_{Zn} concentration estimated from the measured M_s .

In order to understand why such a high V_{Zn} concentration is present in the ILE-grown ZnO nanosheets, DFT calculations were performed on bulk, surface, and grain boundary structures of ZnO to examine the formation energy and magnetic properties of dilute and high (33%) concentrations of V_{Zn} defects unpassivated and passivated with hydrogen. Details of the DFT calculations can be found in Sections 8–12 of the Supporting Information. As shown in Figure 4c, a series of key findings regarding the behavior of V_{Zn} in ZnO have emerged from these calculations. In general, V_{Zn} tends to form more easily in grain boundaries than in the bulk. Further, the

formation energy of V_{Zn} tends to either be similar between surface and bulk (e.g., unpassivated 33% V_{Zn}) or form more easily in surface than in bulk (e.g., H-passivated dilute V_{Zn}).^{34,39,40} Dilute, unpassivated V_{Zn} results in a magnetic moment of $2 \mu_{\text{B}}/V_{\text{Zn}}$, but has high formation energies of 3.75 eV/ V_{Zn} (bulk) and 3.85 eV/ V_{Zn} (surface) at $T = 298$ K and $p(\text{O}_2) = 0.2$ atm. Unpassivated V_{Zn} with a high concentration of 33% also has a magnetic moment of $2 \mu_{\text{B}}/V_{\text{Zn}}$ and results in lowered formation energies compared to bulk by about 800 meV/ V_{Zn} (bulk) and 950 meV/ V_{Zn} (surface). These formation energies of 33% V_{Zn} concentration, while lower than the dilute V_{Zn} formation energies, are not low enough to expect any concentration significant on the scale of the measured magnetism to form at room temperature. However, introduction of H into V_{Zn} to passivate the dangling O bonds (forming a $V_{\text{Zn}} + 2\text{H}$ defect) dramatically reduces the formation energies on the scale of ~ 3 eV/ V_{Zn} (at $T = 298$ K and $p(\text{O}_2) = 0.2$ atm, and in equilibrium with water). In particular, for bulk ZnO with 33% V_{Zn} , these defects may form spontaneously under the synthesis conditions in aqueous solution (four 33% V_{Zn} arrangements were simulated, the average formation energy was 0.01 eV/ V_{Zn} , and two of these arrangements showed negative formation energy of -0.02 eV/ V_{Zn} , see Section S12 of the Supporting Information for more details). Here, our DFT calculations show the passivated $V_{\text{Zn}} + 2\text{H}$ has zero magnetic moment. The elimination of the magnetic moment with H-passivation is expected as the dangling bonds (localized holes) that result from the V_{Zn} are now passivated (filled) by electrons from H. Simple equilibrium thermodynamics and DFT energetics therefore predict that the as-synthesized ZnO should have a very large concentration of passivated non-magnetic $V_{\text{Zn}} + 2\text{H}$, which could be transformed to being magnetically active by annealing out the H to leave unpassivated metastable V_{Zn} . This prediction is consistent with the experimental finding that as-synthesized ZnO nanosheets did not show any ferromagnetism (Figure 4d, V_{Zn} present as passivated $V_{\text{Zn}} + 2\text{H}$) and that strong magnetization emerged after 1 h of annealing in argon at $T = 400$ °C (H removed, V_{Zn} present as unpassivated V_{Zn}). A number of previous experimental studies have also shown that H can be removed from ZnO by annealing at comparable temperatures for 30–60 min in argon or vacuum.^{41–44} The proposed model for $V_{\text{Zn}} + 2\text{H}$ and V_{Zn} defects controlling the magnetism can be further validated by annealing the nanosheets in H_2 . The model implies that further H_2 annealing should remove the ferromagnetism, which is exactly what we observed experimentally (Figure 4e, H added, V_{Zn} once again present as $V_{\text{Zn}} + 2\text{H}$). These modeling and annealing results confirmed that H-passivation plays a critical role in controlling the formation and activation of the V_{Zn} -related ferromagnetism in the nanosheets.

The very high magnetism observed (Figure 4f) can be thought of as having two major sources, bulk V_{Zn} stability and grain boundary interface effects. With regard to bulk stability, the DFT studies show that in equilibrium with an air exposed aqueous environment, even bulk ZnO should form high $V_{\text{Zn}} + 2\text{H}$ concentrations (e.g., close to 33%, the approximate value verified from EELS measurements) and that these defects can be activated to have significant magnetic moments by simple Ar annealing to remove the H. The fact that these high defect concentrations and their associated magnetism have only first been observed here is likely due to the non-equilibrium growth kinetics of ILE and the nanoscale sheets. With regard to the

interfacial effects, the change in magnetic moment measured in this work when changing from single crystal (37.2 emu/g) to polycrystalline (57.2 emu/g) ZnO nanosheets is consistent with grain boundaries increasing the stability of $V_{\text{Zn}} + 2\text{H}$, as predicted by the DFT calculation results shown in Figure 4c. These results suggest that, in general, increasing the fraction of interfacial ZnO through grain boundaries is likely to significantly increase the $V_{\text{Zn}} + 2\text{H}$ concentration, and the corresponding V_{Zn} concentration and associated magnetism after annealing.

In summary, this study has realized an unprecedented concentration of Zn cation vacancies in ZnO (Zn:O ratio of about 2:3, indicating $\sim 33\%$ V_{Zn}) and thereby demonstrated the highest ever recorded saturation magnetization in ZnO at room temperature of 50.9 emu/g, which is comparable to the state-of-the-art ferrimagnetic nanomaterials such as Fe_3O_4 nanoparticles and MnSe_2 2D material. DFT calculations showed that H-passivated V_{Zn} in 33% concentration is likely stable in bulk ZnO under the growth conditions, and EELS measurements confirmed the approximate 2:3 Zn:O ratio. We believe the fast kinetics of the ILE synthesis and the extremely thin ZnO nanosheets enabled the formation of the high V_{Zn} concentrations. Additionally, DFT showed that V_{Zn} may be further stabilized by the grain boundaries in polycrystalline ZnO nanosheets, explaining the higher magnetization of polycrystalline versus monocrystalline ZnO nanosheets. A combination of experimental observations and DFT calculations suggested that the presence of H is essential to stabilizing the high concentration of V_{Zn} during synthesis and that the H has to be removed in order for the nanosheets to show ferromagnetism. Following the same stabilization mechanism, there might be other approaches that can stabilize the Zn vacancies in ILE system, for example, Li ion or Na ion, which could bring more flexibility to develop a defect-controlled system with exotic physical properties. The mechanisms identified for the origin of the high magnetism in ZnO nanosheets suggest that they could be utilized to develop a family of magnetic semiconductor oxides or related materials. While a number of oxides have already been shown to yield magnetic cation vacancies (e.g., ZnO, CaO, MgO, Al_2O_3 , TiO_2)^{45–47} and anion vacancies (e.g., TiO_2 , SnO_2 , HfO_2 , In_2O_3),^{48–50} less is known about how the magnetically active vacancies can be stabilized at reasonably high concentration. For promising materials, synthesis and processing conditions with adequate H and O activity and good equilibration enabled by fast growth kinetics, like ILE, can be explored to yield desired magnetic properties. This discovery may eventually lead to a new class of high saturation moment magnetic semiconducting oxide materials that hold great promise for 2D spintronic and other magnetic applications.

Experimental Section. Synthesis at Water–Oil Interface and Water–Air Interface. In a typical synthesis, the aqueous solution containing 25 mM zinc nitrate ($\text{Zn}(\text{NO}_3)_2$) and hexamethylenetetramine (HMT) was prepared in a 20 mL glass vial. Eight μL of chloroform solution of sodium oleyl sulfate (~ 0.1 vol %) was dispersed on the surface of the precursor solution. Twenty min was allowed for the evaporation of the chloroform and the formation of the surfactant monolayer at the water–air interface. Subsequently, 500 mL of toluene (hexane or cyclohexane) was added to the top of the solution. The glass vial was then capped to form a closed reaction environment and placed in a 60 °C convection oven for the growth of ZnO nanosheets. One h and 45 min

later, the growth was terminated by removing the glass vial from the oven and cooling down to room temperature naturally. The as-prepared ZnO nanosheets were transferred onto a Si substrate with thermal oxide by scooping at the surface of the reaction solution.

Characterization. Zeiss LEO 1530 field-emission scanning electron microscope (SEM) was used to study the morphologies of the nanosheets. Atomic force microscopy (AFM) tomography images were obtained using an XE-70 Park System. X-ray photoelectron spectroscopy (XPS) spectrum was obtained from a Thermo Scientific K-alpha XPS instrument with a 100 μm spot size, with the flood gun turned on during the measurements. FEI TF30 transmission electron microscope (TEM) operated at 300 kV was used to study the crystal structure. Focused ion beam (FIB, Zeiss Auriga) was used to prepare cross section scanning transmission electron microscopy (STEM) samples. The final FIB milling voltage of 5 kV was used to minimize the damage from Ga ion beam. STEM images and EELS spectra were obtained on an FEI Titan with CEOS probe aberration corrector operated at 200 kV with a probe convergence angle of 24.5 mrad, spatial resolution of 0.08 nm, and probe current of ~ 70 pA for STEM imaging and ~ 150 pA for EELS. The superconducting quantum interference device (SQUID) quantum Design MPMS3 magnetometer was used for the measurements of the magnetization as a function of applied magnetic field at both 5 and 300 K. The magnetic property of ZnO nanosheets was measured from a monolayer of densely distributed nanosheets supported on single-crystalline Al_2O_3 substrates. The coverage and distribution of ZnO nanosheets obtained from water–air and water–oil interfaces were first characterized by SEM. Statistical measurements from five randomly selected areas of $150 \times 250 \mu\text{m}^2$ gave the surface coverage of $60.1 \pm 2.6\%$ and $62.7 \pm 3.1\%$ (errors are standard deviation between the measurements) for the water–air and water–oil nanosheets, respectively, which correspond to $9.9 \pm 1.7 \times 10^{-7}$ and $6.5 \pm 0.7 \times 10^{-7}$ g/cm². The magnetic field was applied parallel to the nanosheets. The temperature-dependent magnetization was further probed by the zero field cooled (ZFC) and field cooled (FC) measurements, in which the samples were cooled to 5 K without and with a magnetic field of 500 Oe, respectively, and subsequently the magnetization was recorded when raising the temperature from 5 to 300 K under the same magnetic field.

■ ASSOCIATED CONTENT

■ Supporting Information

The Supporting Information is available free of charge on the ACS Publications website at DOI: 10.1021/acs.nanolett.9b02581.

Details on the methods of synthesis and characterizations, discussion about the growth using other oil phases, molecular simulation, DFT calculation details, ZnO defect calculations and thermodynamic formalism, and calculated defect formation energies and magnetic moments in ZnO bulk, surface, and grain boundary structures (PDF)

■ AUTHOR INFORMATION

Corresponding Author

*E-mail: xudong.wang@wisc.edu.

ORCID

Xin Yin: 0000-0002-4759-0226

Yizhan Wang: 0000-0003-0464-6610

Ryan Jacobs: 0000-0003-2229-6730

Izabela Szlufarska: 0000-0002-5895-8620

Dane Morgan: 0000-0002-4911-0046

Xudong Wang: 0000-0002-9762-6792

Author Contributions

X.Y. and X.W. conceived the idea and designed the experiments. X.Y. performed the synthesis and the characterizations of the samples. X.Y. and Y.W. measured the magnetic properties. Y.S. and I.S. conducted the molecular simulation on the distribution profiles of the charge density and Zn^{2+} ions concentration from the interface to the bulk solution. R.J. and D.M. did the DFT calculations on the formation energy and magnetic properties of Zn vacancy defects. X.W. and X.Y. wrote the manuscript. All the authors discussed the results, commented on the manuscript, and approved to the final version of the manuscript.

Author Contributions

[†]These authors contributed equally.

Notes

The authors declare no competing financial interest.

■ ACKNOWLEDGMENTS

This work was primarily supported by Army Research Office (ARO) under grant W911NF-16-1-0198 and National Science Foundation DMR-1709025. The authors would like to thank Ymir Frodason for the helpful discussions and Christian Elsässer for providing the grain boundary structure files. Funding for D.M. and R.J. for this work was provided by the NSF Software Infrastructure for Sustained Innovation (SI2) award no. 1148011. Computational support was provided by the Extreme Science and Engineering Discovery Environment (XSEDE), which is supported by National Science Foundation grant no. OCI-1053575. I.S. and Y.S. gratefully acknowledge support from the Army Research Office grant ARO W911NF-17-1-0571. The Quantum Design MPMS3 magnetometer was supported by the Department of Chemistry, University of Wisconsin-Madison.

■ REFERENCES

- (1) Fang, J.; Fan, H.; Ma, Y.; Wang, Z.; Chang, Q. *Appl. Surf. Sci.* **2015**, *332*, 47–54.
- (2) Kang, J.; Wang, L.-W. *J. Phys. Chem. Lett.* **2017**, *8* (2), 489–493.
- (3) Queisser, H. J.; Haller, E. E. *Science* **1998**, *281* (5379), 945–950.
- (4) Kayaci, F.; Vempati, S.; Donmez, I.; Biyikli, N.; Uyar, T. *Nanoscale* **2014**, *6* (17), 10224–10234.
- (5) Zeng, H.; Duan, G.; Li, Y.; Yang, S.; Xu, X.; Cai, W. *Adv. Funct. Mater.* **2010**, *20* (4), 561–572.
- (6) Nowotny, J.; Alim, M. A.; Bak, T.; Idris, M. A.; Ionescu, M.; Prince, K.; Sahdan, M. Z.; Sopian, K.; Mat Teridi, M. A.; Sigmund, W. *Chem. Soc. Rev.* **2015**, *44* (23), 8424–8442.
- (7) Janotti, A.; Van de Walle, C. G. *J. Cryst. Growth* **2006**, *287* (1), 58–65.
- (8) Xu, Q.; Schmidt, H.; Zhou, S.; Potzger, K.; Helm, M.; Hochmuth, H.; Lorenz, M.; Setzer, A.; Esquinazi, P.; Meinelcke, C.; Grundmann, M. *Appl. Phys. Lett.* **2008**, *92* (8), 082508.
- (9) Khalid, M.; Ziese, M.; Setzer, A.; Esquinazi, P.; Lorenz, M.; Hochmuth, H.; Grundmann, M.; Spemann, D.; Butz, T.; Brauer, G.; et al. *Phys. Rev. B: Condens. Matter Mater. Phys.* **2009**, *80* (3), 035331.
- (10) Adeagbo, W.; Fischer, G.; Ernst, A.; Hergert, W. *J. Phys.: Condens. Matter* **2010**, *22* (43), 436002.

- (11) Xing, G.; Lu, Y.; Tian, Y.; Yi, J.; Lim, C.; Li, Y.; Li, G.; Wang, D.; Yao, B.; Ding, J.; et al. *AIP Adv.* **2011**, *1* (2), 022152.
- (12) Kapilashrami, M.; Xu, J.; Ström, V.; Rao, K. V.; Belova, L. *Appl. Phys. Lett.* **2009**, *95* (3), 033104.
- (13) Peng, C.; Liang, Y.; Wang, K.; Zhang, Y.; Zhao, G.; Wang, Y. *J. Phys. Chem. C* **2012**, *116* (17), 9709–9715.
- (14) Peng, C.; Wang, Y.; Cheng, Z.; Zhang, G.; Wang, C.; Yang, G. *Phys. Chem. Chem. Phys.* **2015**, *17* (25), 16536–16544.
- (15) Wu, J.; Tang, X.; Long, F.; Tang, B. *Phys. Status Solidi B* **2017**, *254* (6), 1600838.
- (16) Yin, Y.; Alivisatos, A. P. *Nature* **2005**, *437* (7059), 664–670.
- (17) Peng, Y.-K.; Tsang, S. C. E. *Nano Today* **2018**, *18*, 15–34.
- (18) Xu, S. J.; Li, G.; Chua, S. J.; Wang, X. C.; Wang, W. *Appl. Phys. Lett.* **1998**, *72* (19), 2451–2453.
- (19) Yang, D.-Q.; Rochette, J.-F.; Sacher, E. *Langmuir* **2005**, *21* (18), 8539–8545.
- (20) Ischenko, V.; Polarz, S.; Grote, D.; Stavarache, V.; Fink, K.; Driess, M. *Adv. Funct. Mater.* **2005**, *15* (12), 1945–1954.
- (21) Wang, F.; Yin, X.; Wang, X. *Extreme Mechanics Letters* **2016**, *7*, 64–70.
- (22) Yin, X.; Shi, Y.; Wei, Y.; Joo, Y.; Gopalan, P.; Szlufarska, I.; Wang, X. *Langmuir* **2017**, *33* (31), 7708–7714.
- (23) Li, M.; Acero, A. A.; Huang, Z.; Rice, S. A. *Nature* **1994**, *367* (6459), 151–153.
- (24) Yang, J.; Meldrum, F. C.; Fendler, J. H. *J. Phys. Chem.* **1995**, *99* (15), 5500–5504.
- (25) Gidalevitz, D.; Weissbuch, I.; Kjaer, K.; Als-Nielsen, J.; Leiserowitz, L. *J. Am. Chem. Soc.* **1994**, *116* (8), 3271–3278.
- (26) Wang, J.; Hou, S.; Chen, H.; Xiang, L. *J. Phys. Chem. C* **2014**, *118* (33), 19469–19476.
- (27) Garcia, M.; Merino, J.; Fernández Pinel, E.; Quesada, A.; De la Venta, J.; Ruíz González, M.; Castro, G.; Crespo, P.; Llopis, J.; González-Calbet, J.; et al. *Nano Lett.* **2007**, *7* (6), 1489–1494.
- (28) Sharma, P.; Gupta, A.; Rao, K.; Owens, F. J.; Sharma, R.; Ahuja, R.; Guillen, J. O.; Johansson, B.; Gehring, G. *Nat. Mater.* **2003**, *2* (10), 673.
- (29) Li, Z.; Zhong, W.; Li, X.; Zeng, H.; Wang, G.; Wang, W.; Yang, Z.; Zhang, Y. *J. Mater. Chem. C* **2013**, *1* (41), 6807–6812.
- (30) O'Hara, D. J.; Zhu, T.; Trout, A. H.; Ahmed, A. S.; Luo, Y. K.; Lee, C. H.; Brenner, M. R.; Rajan, S.; Gupta, J. A.; McComb, D. W.; et al. *Nano Lett.* **2018**, *18* (5), 3125–3131.
- (31) Li, B.; Xing, T.; Zhong, M.; Huang, L.; Lei, N.; Zhang, J.; Li, J.; Wei, Z. *Nat. Commun.* **2017**, *8* (1), 1958.
- (32) Wei, Y.; Han, B.; Hu, X.; Lin, Y.; Wang, X.; Deng, X. *Procedia Eng.* **2012**, *27*, 632–637.
- (33) Khalid, M.; Ziese, M.; Setzer, A.; Esquinazi, P.; Lorenz, M.; Hochmuth, H.; Grundmann, M.; Spemann, D.; Butz, T.; Brauer, G.; Anwand, W.; Fischer, G.; Adeagbo, W. A.; Hergert, W.; Ernst, A. *Phys. Rev. B: Condens. Matter Mater. Phys.* **2009**, *80* (3), 035331.
- (34) Xing, G. Z.; Lu, Y. H.; Tian, Y. F.; Yi, J. B.; Lim, C. C.; Li, Y. F.; Li, G. P.; Wang, D. D.; Yao, B.; Ding, J.; Feng, Y. P.; Wu, T. *AIP Adv.* **2011**, *1* (2), 022152.
- (35) Tan, C.; Cao, X.; Wu, X.-J.; He, Q.; Yang, J.; Zhang, X.; Chen, J.; Zhao, W.; Han, S.; Nam, G.-H.; Sindoro, M.; Zhang, H. *Chem. Rev.* **2017**, *117* (9), 6225–6331.
- (36) Adeagbo, W. A.; Fischer, G.; Ernst, A.; Hergert, W. *J. Phys.: Condens. Matter* **2010**, *22* (43), 436002.
- (37) Lin, Q. L.; Li, G. P.; Xu, N. N.; Liu, H.; E, D. J.; Wang, C. L. *J. Chem. Phys.* **2019**, *150* (9), 094704.
- (38) Wu, J.; Tang, X.; Long, F.; Tang, B. *Phys. Status Solidi B* **2017**, *254* (6), 1600838.
- (39) Wang, Q.; Sun, Q.; Chen, G.; Kawazoe, Y.; Jena, P. *Phys. Rev. B: Condens. Matter Mater. Phys.* **2008**, *77* (20), 205411.
- (40) Hong, N. H.; Sakai, J.; Brizé, V. *J. Phys.: Condens. Matter* **2007**, *19* (3), 036219.
- (41) Lavrov, E.; Weber, J.; Börrnert, F.; Van de Walle, C. G.; Helbig, R. *Phys. Rev. B: Condens. Matter Mater. Phys.* **2002**, *66* (16), 165205.
- (42) Shi, G. A.; Stavola, M.; Pearton, S.; Thieme, M.; Lavrov, E.; Weber, J. *Phys. Rev. B: Condens. Matter Mater. Phys.* **2005**, *72* (19), 195211.
- (43) Lee, S.; Lee, T.; Lee, K.; Cheong, B.; Kim, Y.; Kim, W. *J. Phys. D: Appl. Phys.* **2008**, *41* (9), 095303.
- (44) Ip, K.; Overberg, M.; Heo, Y.; Norton, D.; Pearton, S.; Kucheyev, S.; Jagadish, C.; Williams, J.; Wilson, R.; Zavada, J. *Appl. Phys. Lett.* **2002**, *81* (21), 3996–3998.
- (45) Wang, S.; Pan, L.; Song, J.-J.; Mi, W.; Zou, J.-J.; Wang, L.; Zhang, X. *J. Am. Chem. Soc.* **2015**, *137* (8), 2975–2983.
- (46) Gao, D.; Li, J.; Li, Z.; Zhang, Z.; Zhang, J.; Shi, H.; Xue, D. *J. Phys. Chem. C* **2010**, *114* (27), 11703–11707.
- (47) Li, J.; Jiang, Y.; Li, Y.; Yang, D.; Xu, Y.; Yan, M. *Appl. Phys. Lett.* **2013**, *102* (7), 072406.
- (48) Sundaresan, A.; Bhargavi, R.; Rangarajan, N.; Siddesh, U.; Rao, C. *Phys. Rev. B: Condens. Matter Mater. Phys.* **2006**, *74* (16), 161306.
- (49) Hong, N. H.; Sakai, J.; Poirrot, N.; Brizé, V. *Phys. Rev. B: Condens. Matter Mater. Phys.* **2006**, *73* (13), 132404.
- (50) Hong, N. H.; Poirrot, N.; Sakai, J. *Phys. Rev. B: Condens. Matter Mater. Phys.* **2008**, *77* (3), 033205.
- (51) Tietze, T.; Audehm, P.; Chen, Y. C.; Schütz, G.; Straumal, B. B.; Protasova, S. G.; Mazilkin, A. A.; Straumal, P. B.; Prokscha, T.; Luetkens, H. *Sci. Rep.* **2015**, *5*, 8871.
- (52) Hong, J.-I.; Choi, J.; Jang, S. S.; Gu, J.; Chang, Y.; Wortman, G.; Snyder, R. L.; Wang, Z. L. *Nano Lett.* **2012**, *12* (2), 576–581.
- (53) Gong, C.; Li, L.; Li, Z.; Ji, H.; Stern, A.; Xia, Y.; Cao, T.; Bao, W.; Wang, C.; Wang, Y. *Nature* **2017**, *546* (7657), 265.
- (54) Bonilla, M.; Kolekar, S.; Ma, Y.; Diaz, H. C.; Kalappattil, V.; Das, R.; Eggers, T.; Gutierrez, H. R.; Phan, M.-H.; Batzill, M. *Nat. Nanotechnol.* **2018**, *13* (4), 289.